

Using krypton-83m to determine the neutrino-mass bias caused by a non-constant electric potential of the KATRIN source

Moritz Machatschek^{a,1}

¹This work was largely conducted while the author was affiliated with Institute for Astroparticle Physics (IAP), Karlsruhe Institute of Technology (KIT), Hermann-von-Helmholtz-Platz 1, 76344 Eggenstein-Leopoldshafen, Germany

Received: date / Accepted: date

Abstract Precision spectroscopy of the electron spectrum of the tritium β decay near the kinematic endpoint is a direct method to determine the effective electron antineutrino mass. The Karlsruhe Tritium Neutrino (KATRIN) experiment aims to determine this quantity with a sensitivity of better than 0.3 eV (90 % C.L.). An inhomogeneous electric potential in the tritium source of KATRIN leads to a distortion of the β spectrum, which directly impacts the neutrino-mass observable. This effect can be quantified through precision spectroscopy of the conversion electrons of co-circulated metastable $^{83\text{m}}\text{Kr}$. This work perturbatively describes the effect of the source potential on the recorded spectra, and thus establishes the leading-order observables of this effect.

1 Introduction

While neutrino-oscillation experiments show that neutrinos have mass [1, 2], the absolute mass scale of neutrinos remains unknown. The Karlsruhe Tritium Neutrino (KATRIN) experiment is the latest experiment in the field of direct neutrino-mass measurements with the goal to determine the absolute neutrino-mass scale, currently providing the best laboratory neutrino-mass upper limit of 0.45 eV/c² (90 % confidence level (C.L.)) [3]. KATRIN uses high-precision electron spectroscopy to perform a shape analysis of the tritium β spectrum near the kinematic endpoint at 18.6 keV, where the imprint of a non-vanishing neutrino mass is the most pronounced. Any other influence on the β spectrum shape in this region has to be well understood, since it would otherwise lead to a systematic bias of the neutrino-mass measurement. Thus, reaching the target sensitivity of better than 0.3 eV/c² at 90 % C.L. requires the detailed study of systematic measurement uncertainties.

One major uncertainty is linked to the electric potential inside the tritium source. Inhomogeneities of the potential lead to a distribution of starting energies of the β electrons and thus to a distortion of the β spectrum, which needs to be characterized in order to reduce the systematic bias in the neutrino-mass measurement.

To this end, conversion electrons from $^{83\text{m}}\text{Kr}$ are used as nuclear standard. In dedicated calibration measurements, traces of gaseous $^{83\text{m}}\text{Kr}$ are circulated alongside tritium in the 10 m long source, such that inhomogeneities of the potential are observable as distortion of the selected mono-energetic $^{83\text{m}}\text{Kr}$ lines.

The focus of this work is to derive the leading-order effects caused by the electric potential; in section 2, the statistical moments of the potential, which are direct observables in the $^{83\text{m}}\text{Kr}$ measurement, and relations between these moments, given the special properties of the KATRIN source. In section 3, the systematic biases of the observable neutrino mass and β spectrum endpoint as function of these moments. Section 4 contains relevant supplements, which go beyond the main discussion.

2 The starting potential in the KATRIN model

In the following, the relevant components of the KATRIN model are described and the essential mechanism for incorporating the potential is identified. Then, the leading-order observables of the potential are derived and their connection to the potential shape is established. Natural units with $c = e = 1$ are used throughout the paper.

^ae-mail: moritz.machatschek@web.de

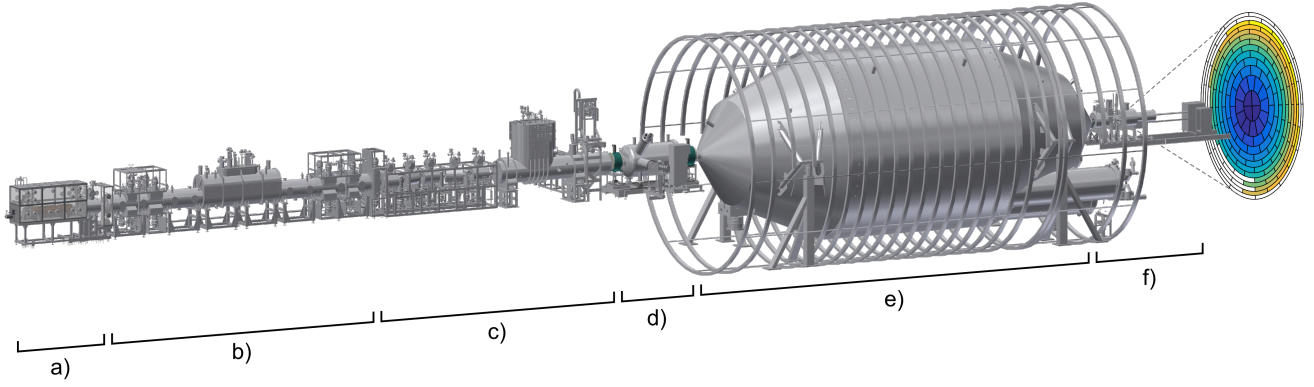


Fig. 1: Schematic of the KATRIN beamline with FPD. The rear section a) is used for calibration and monitoring. The decay of gaseous tritium or krypton-83m takes place in the source b). Since the source is windowless, the gas is removed in the transport section c) using differential pumping and cryosorption, while the decay electrons are guided adiabatically to the spectrometer section d) and e) by a strong magnetic field. Electrons that can overcome the retarding potential of the main spectrometer e) are counted at the focal plane detector f). The segmentation of the focal plane detector in 148 pixels (shown on the right) and the magnetic guidance allow for radial resolution of the measurement, in particular of the source.

2.1 The KATRIN model

A schematic of the KATRIN experiment is shown in figure 1. The reader is referred to [4] for a detailed description of the components and to [5] for details on the modeling.

Electrons are created by the β decay of T_2 or internal conversion of ^{83m}Kr inside the Windowless Gaseous Tritium Source (WGTS, figure 1b)), which is a cylinder of 4.5 cm radius and $L = 10$ m length. The electrons are guided through the experiment by a strong magnetic field. Radial variances in the physical quantities, like the electric potential of the axially-symmetric experiment, are mapped to distinct pixels of the Focal Plane Detector (FPD, figure 1f)) by the magnetic field and are not considered in the following. However, longitudinal inhomogeneities (coordinate z) along one field line are integrated into a distorted spectrum, measured by one pixel. Determining this distortion caused by an unknown electric potential $V(z)$ in leading order is the goal of this paper. For ease of notation the z -integration is written as

$$\int \frac{dz}{L} \dots \equiv \langle \dots \rangle . \quad (1)$$

in this section. Further integral operators are defined below using square brackets. Accordingly, since arguments in $\langle \dots \rangle$ and $[\dots]$ are always z -dependent functions, the z -dependency is often omitted. Arguments in (\dots) are always scalars.

KATRIN uses an electrostatic spectrometer of the MAC-E filter (magnetic adiabatic collimation with electro-static filter) type (figure 1e)) for the energy spectroscopy: only electrons (charge $q = -1$) with energies in forward direction larger than the retarding energy qU (with retarding potential U) applied at the spectrometer can pass to the detector and get counted, all other electrons are reflected. Thus,

the transmission condition $\mathcal{T}(E, \theta, U)$ is a function of the electron energy E , the retarding potential and the angle θ of the electron with regard to the magnetic field. By lowering the magnetic field inside the MAC-E filter by several orders of magnitude compared to the magnetic field in the source, the electron angles are collimated in forward direction. As a consequence, the transmission condition implicitly also depends on the ratio of the magnetic fields, as well as on higher order corrections like synchrotron radiation and relativistic effects among others. In order to avoid systematic effects, electrons with angles larger than $\theta_{\max} \approx 51^\circ$ are cut off. This is achieved using the magnetic mirror effect, by applying the strongest magnetic field directly in front of the detector.

The spectrum of the electrons gets modified by inelastic scattering of the electrons on the gas. Thereby the electrons lose the energy ε with a probability density $f(\varepsilon)$. Multiple scattering events with multiplicity i are described by convolving the so-called energy-loss function with itself

$$f_i = \underbrace{\delta \otimes f \otimes f \dots}_{i\text{-times}} , \quad (2)$$

where δ is the δ distribution.

The probability $p_i(E, \theta, z)$ of scattering i times is given by [5]

$$p_i(E, \theta, z) = \frac{(\mathcal{N}_{\text{eff}}(\theta, z) \sigma_{\text{tot}}(E))^i}{i!} e^{-\mathcal{N}_{\text{eff}}(\theta, z) \sigma_{\text{tot}}(E)} . \quad (3)$$

It depends on the electron energy via the scattering cross section $\sigma_{\text{tot}}(E)$, and on the effective gas column density [5]

$$\mathcal{N}_{\text{eff}}(\theta, z) = \frac{1}{\cos \theta} \int_z^{L/2} \rho(z') dz' \quad (4)$$

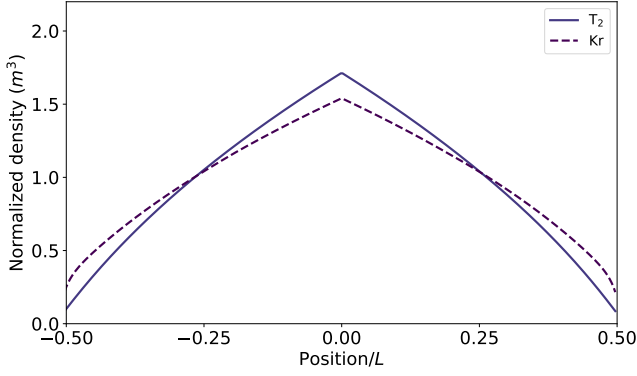


Fig. 2: Longitudinal density profile in the source. The gas gets injected in the center and evacuated towards both ends of the source. Here, the densities are normalized, while the density of $^{83\text{m}}\text{Kr}$ is usually around 9 orders of magnitude smaller than that of T_2 [6]. Due to the larger mass of $^{83\text{m}}\text{Kr}$ it accumulates at both ends of the source compared to T_2 . The densities were calculated following the models explained in [7, 8].

an electron needs to traverse, where $\rho(z)$ is the density of the gas. Both a higher angle θ and a longitudinal starting position z towards the rear of the source lead to a larger effective path length and thus to a higher probability of scattering.

The source strength at KATRIN is usually quantified using the column density $\mathcal{N} = \mathcal{N}_{\text{eff}}(\theta = 0, z = -L/2)$. To account for the longitudinal distribution of the electron emitters, the normalized density $\bar{\rho}(z) = \frac{\rho(z)}{\mathcal{N}/L}$ is used. As shown in figure 2, since the gas is injected at the center of the source and evacuated at both ends, the profile of the density is approximately triangular. For the measurements discussed in this work, gas mixtures of T_2 and $^{83\text{m}}\text{Kr}$ are used, where the density of gaseous $^{83\text{m}}\text{Kr}$ is many orders of magnitude lower than that of T_2 . Thus, while the rate of the T_2 and $^{83\text{m}}\text{Kr}$ spectra are proportional to their respective densities, the scattering probabilities are always calculated using the T_2 density.

As stated initially, the spectrum measured in a single pixel is proportional to the total number of electrons emitted along a magnetic field line. To perform the corresponding integration, all z -dependent quantities must be taken into account. In this section, only the scattering probabilities and the gas density are considered, while the influence of other effects is discussed in section 4.1. In the absence of an electric potential, the integration over z yields the weighted scattering probabilities

$$\bar{p}_i(E, \theta) \equiv \langle \bar{\rho}(z) p_i(E, \theta, z) \rangle, \quad (5)$$

which appear as an overall factor in the rate calculation.

To describe the transmission probability of an electron of energy E , given the retarding potential U , the source scatter-

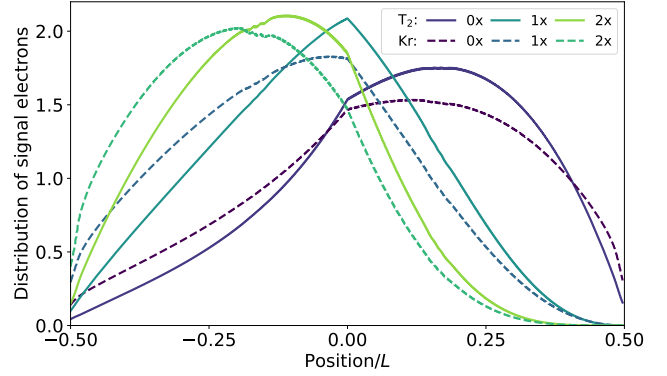


Fig. 3: Distribution of electrons in the gaseous source. The electron distributions $P_i(z)$ are dominated by the z -dependent scattering probabilities (multiplicity 0x, 1x, 2x) and the gas density. A small, additional effect stems from a slight decrease of the source magnetic field due to gaps between the coils, causing the ripples visible around $\pm 0.2 L$ (c.f. section 4.1). The source conditions of the KATRIN measurement campaigns since KNM3-NAP (c.f. table 1) have been used. The magnetic field and scattering probabilities were calculated following the models explained in [5, 8].

ing and transmission properties of the MAC-E filter are then combined into the so-called response function

$$R(E, U) = \sum_i R_i(E, U), \quad (6)$$

where the response function for each scattering (c.f. equations 20 and 24 in [5])¹

$$R_i(E, U) \equiv \int_{\theta=0}^{\theta_{\max}} d\theta \sin \theta (\bar{p}_i \mathcal{T} \otimes f_i)(E, \theta, U) \quad (7)$$

is understood as follows. T_2 and $^{83\text{m}}\text{Kr}$ are isotropical electron sources. Therefore, the number of electrons with starting angle θ is proportional to $\sin \theta \bar{p}_i(E, \theta)$. The electrons are transmitted and counted in a single pixel if the transmission condition $\mathcal{T}(E, \theta, U)$ is fulfilled and if θ does not exceed the maximum allowed angle θ_{\max} . The spectrum of the electrons is modified by the inelastic scattering with probability density f_i .

Using the decay rate $\frac{d\dot{N}}{dE}(E)$ of one T_2 molecule or $^{83\text{m}}\text{Kr}$ atom, the measured count rate is then calculated as

$$\dot{N}(U) \propto \mathcal{N} \int_{-\infty}^{\infty} dE \frac{d\dot{N}}{dE}(E) R(E, U). \quad (8)$$

The constant of proportionality contains z -independent factors, that are irrelevant in the context of this work.

¹To save on space, in some cases the arguments (E, θ, U) are put at the end of the equation. The actual dependencies should be clear from the text.

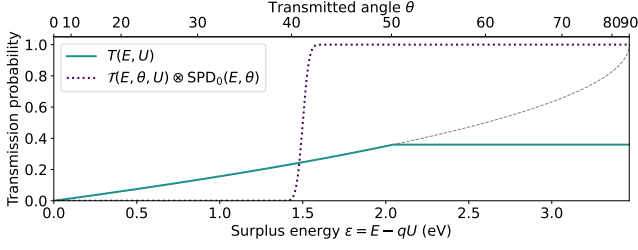


Fig. 4: Transmission function. This plot illustrates equation 11. The transmission condition is a step function in the surplus energy, corresponding to the energy required for electrons at a given angle to be transmitted. It is modified by the potential distribution, here modeled as a Gaussian, which may also depend on the angle due to the weighting with the signal electron distributions. For unscattered electrons, the transmission function is obtained by integrating this broadened step function over the angle, taking into account the phase space factor $\sin \theta$, $\bar{p}_0(E, \theta)$. The integration is cut at the maximum angle of around 51° . The plot shows typical settings used for the $^{83\text{m}}\text{Kr}$ measurement.

When the starting potential $V(z)$ is introduced, the transmission condition needs to be modified and the z -integration needs to include the potential, leading to the modified response function

$$R'_i(E, U) = \int_{\theta=0}^{\theta_{\max}} d\theta \sin \theta (\bar{p}_i \langle P_i \mathcal{T}(U - V) \rangle \otimes f_i)(E, \theta), \quad (9)$$

with the normalized electron distributions

$$P_i(E, \theta, z) \equiv \frac{\bar{p}(z) p_i(E, \theta, z)}{\bar{p}_i(E, \theta)}. \quad (10)$$

These distributions quantify the regions in which the measurement is sensitive to the starting potential, given the energy, angle, and scattering multiplicity of the electrons. They are shown in figure 3, using scattering probabilities averaged over θ . The difference between T_2 and $^{83\text{m}}\text{Kr}$ arises not only from their different density profiles, but also from the fact that different energy ranges are used in the measurements (β spectrum endpoint $E_0 \approx 18.6 \text{ keV}$, $^{83\text{m}}\text{Kr}$ lines at $\approx 32.1 \text{ keV}$). This results in a different inelastic scattering cross section. Consequently, the spectra of the two species are affected by the starting potential with different weights, leading to uncertainties discussed in section 4.3.

2.2 Starting-potential distributions

By inserting an integral over a δ distribution or using variable transformation, equation 9 can be rewritten using an

additional convolution

$$R'_i(E, U) = \int_{\theta=0}^{\theta_{\max}} d\theta \sin \theta (\bar{p}_i \mathcal{T} \otimes \text{SPD}_i \otimes f_i)(E, \theta, U) \quad (11)$$

with normalized starting-potential distributions

$$\text{SPD}_i(v, E, \theta) \equiv \langle \delta(v - V(z)) P_i(E, \theta, z) \rangle. \quad (12)$$

They represent the frequency distributions of encountering a potential value v , considering the electron distributions $P_i(E, \theta, z)$.

Equation 11 is visualized in figure 4. It has important implications: The effect of the starting potential is fully described by the starting-potential distributions. Inversely, different starting potentials that lead to the same distributions are non-distinguishable in measured electron spectra. Any measurement of the electron spectrum can only depend on the distributions, but not the z -dependent potential.

In the following, it is assumed that the dependency of the starting potential distributions on the energy and the angle can be neglected:

$$\text{SPD}_i(v) \approx \langle \delta(v - V(z)) P_i(z) \rangle, \quad (13)$$

using the electron distributions approximated as

$$P_i(z) \approx \frac{\bar{p}(z) p_i(z)}{\bar{p}_i}, \quad (14)$$

where the $p_i(z)$ are the scattering probabilities averaged over the angle. This approximation only concerns the sensitive region to the starting potential. It is not applied to the weighted scattering probabilities $\bar{p}_i(E, \theta)$ of equation 11, which are directly proportional to the electron rate. The implications are further discussed in section 4.1.

Since the convolution is both commutative and associative, the starting potential can then be considered as a modification of the energy-loss functions in equation 2

$$f'_i = \text{SPD}_i \underbrace{\otimes f \otimes f \dots}_{i\text{-times}}. \quad (15)$$

Again, this has important implications: For a given scattering multiplicity, the effect of the starting potential is indistinguishable from a modification of the observed energy loss. This is a consequence of the z -dependency of the scattering probabilities, such that electrons with different scattering multiplicities start in different average potentials.

Thus, implementing the SPD_i like in equation 15 is the only change of the KATRIN model necessary to consider the starting potential. In particular, this approach is still correct within the discussed approximations, even if higher order effects for example of the transmission condition are taken into account.

When performing the integration over θ , one obtains the transmission function [5, 9]

$$T_i(E, U) = \int_{\theta=0}^{\theta_{\max}} d\theta \sin \theta \bar{p}_i(E, \theta) \mathcal{T}(E, \theta, U) \quad (16)$$

for each scattering i , which is a step function with a width ΔE on the order of 1 eV. The spectrum is then calculated using the integration of equation 8 and the modified response function

$$R'(E, U) = \sum_i T_i(E, U) \otimes f'_i. \quad (17)$$

2.3 Statistical moments of the starting-potential distributions

To quantify the effect of the starting potential on the spectra, the spectral shape has to be taken into account. Due to the commutativity of the convolution, it is also possible to first perform the energy integration, and afterwards the convolution with the SPD $_i$. This leads to the measured spectrum

$$\dot{N}(U) = \sum_i \dot{N}_i(U) \otimes \text{SPD}_i, \quad (18)$$

with the definition of the i -times scattered spectrum

$$\dot{N}_i(U) \propto \mathcal{N} \int_{-\infty}^{\infty} dE \frac{d\dot{N}}{dE}(E) R_i(E, U). \quad (19)$$

Experimentally, the full SPD $_i$ cannot be determined and, instead, they are approximated by their statistical moments

$$\mu_{n,i}[V] \equiv \langle V^n(z) P_i(z) \rangle. \quad (20)$$

The moments then appear in the calculation of equation 18 by means of the Taylor expansion

$$\dot{N}_i(U) \otimes \text{SPD}_i = \int dv \dot{N}_i(U - v) \text{SPD}_i(v), \quad (21)$$

$$= \sum_{n=0}^{\infty} \frac{\dot{N}_i^{(n)}(U)}{n!} (-1)^n \int dv v^n \text{SPD}_i(v), \quad (22)$$

$$= \sum_{n=0}^{\infty} \frac{\dot{N}_i^{(n)}(U)}{n!} (-1)^n \mu_{n,i}[V]. \quad (23)$$

Here, $\dot{N}_i^{(n)}$ is the n -th derivative of the i -times scattered spectrum with respect to U .

If the derivatives of the spectrum decrease sufficiently fast, the higher-order terms of the expansion can be neglected or treated as biases on the leading order moments. For the tritium spectrum, Slezak argues in [10], that by this logic a second order expansion is sufficient to characterize the neutrino-mass bias, which is further discussed in section 3. Accordingly, in order to characterize the potential-induced

neutrino-mass bias, it is enough to determine the first two moments in the $^{83\text{m}}\text{Kr}$ measurement, i.e. the means

$$\langle V \rangle_i \equiv \int \frac{dz}{L} V(z) P_i(z) \quad (24)$$

and standard deviations

$$\sigma_i[V] \equiv \sqrt{\langle V^2 \rangle_i - \langle V \rangle_i^2}. \quad (25)$$

If the higher moments are neglected, this corresponds to an approximation of the SPD $_i$ with Gaussian distributions $G(\langle V \rangle_i, \sigma_i[V])$. It depends on the remainder term of equation 23 whether neglecting higher moments of the true potential causes a sizable bias on the first two moments in the $^{83\text{m}}\text{Kr}$ measurement. Using Hölder's inequality on the unknown higher moments one can show, that in general the orders $n \geq 3$ are suppressed with $(\frac{\sigma_i}{w})^n$, where w is the characteristic width of the spectrum. For a standard deviation of the potential of around 30 mV [11] and the transmission function width $w \approx \Delta E$ on the 1 eV scale in the $^{83\text{m}}\text{Kr}$ measurement, each subsequent order is suppressed by a factor on the order of 10^{-2} . Further studies are recommended to show, if this suppresses a possible bias of the first two moments sufficiently.

Since a constant potential only shifts the spectra, it is convenient to use $\langle V \rangle_0$ to describe the overall scale of the potential, and to replace the higher $\langle V \rangle_{i>0}$ by the so-called energy-loss shifts

$$\Delta_{i0}[V] \equiv \langle V \rangle_i - \langle V \rangle_0, \quad (26)$$

$$= \int \frac{dz}{L} V(z) [P_i(z) - P_0(z)]. \quad (27)$$

They are the potential induced shift of the i -times scattered spectra compared to the unscattered spectrum. As they vanish for a constant potential, they are measures of the inhomogeneity of the potential.

Describing the influence of the potential by the statistical moments $\langle V \rangle_0$, $\Delta_{i0}[V]$, $\sigma_i[V]$ is the natural, perturbative approach up to the second power of the potential. Up to this order, any observable of the potential has to depend on combinations of these moments. Also, since the energy-loss shifts are a linear order effect, their influence on the measured spectra is in general expected to be larger than that of the standard deviations. The Δ_{i0} exist as a consequence of the electron scattering on the source gas, and were not considered by KATRIN's predecessor experiments.

2.4 Determining the moments: The gaseous $^{83\text{m}}\text{Kr}$ measurement

At KATRIN gaseous krypton-83m is co-circulated alongside tritium for the purpose of calibration measurements [6,

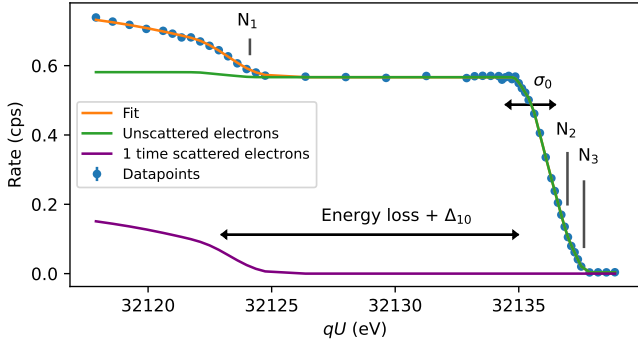


Fig. 5: Krypton-83m N_{23} spectrum with energy loss. The orange line shows a fit of the measured N_{123} spectrum. One-time scattered electrons are visible as a rate increase approximately 13 eV below the main peak (purple). Changes of this distance $\Delta_{10}[V]$ are an observable of the inhomogeneity of the electric potential. Changes of the line width of the non-scattered electrons are given by the standard deviation $\sigma_0[V]$ of the potential. The N_1 line coincides with the scattering and is a nuisance in these measurements. Plot from [11].

[11]. The krypton-83m generates a spectrum of quasi-mono-energetic conversion electrons, which can be used to determine $\langle V \rangle_0$, $\Delta_{10}[V]$ and $\sigma_0^2[V]$. The experimental details and considered sources of error are discussed in [11].

A spectrum of the measurements is found in figure 5. Since the width of the used N_{23} lines can be approximated as zero, the spectrum is essentially a direct measurement of the response function as modified by the starting potential. Electrons lose at least around 13 eV when scattering on the tritium gas, such that in the experimental ^{83m}Kr spectrum the first scattering is directly visible as a line 13 eV below the non-scattered line. Since the scattering introduces a broadening to the scattered spectrum that is orders of magnitude larger than the variance of the source potential, the broadenings $\sigma_{i \geq 1}$ are irrelevant both for the krypton and tritium measurement. In the fit of the ^{83m}Kr spectra usually $\sigma_0 = \sigma_1$ is used, and the measurement range is cut such that no significant contribution from scatterings larger than 1 is observed, as shown in the plot.

The ^{83m}Kr measurement only allows to determine $\Delta_{10}[V]$, but no energy-loss shifts for higher scatterings. Fortunately, since both the $\Delta_{10}[V]$ and the $\sigma_i[V]$ are a measure of inhomogeneity of the potential, the allowed parameter space of all the $\Delta_{10}[V]$ is already constrained by one measured $\sigma_j[V]$. This is shown in the following.

2.5 Relation of the moments to the potential shape

In this section, relations between the observables Δ_{10} and σ_0 are derived. This section generalizes findings from [6] up

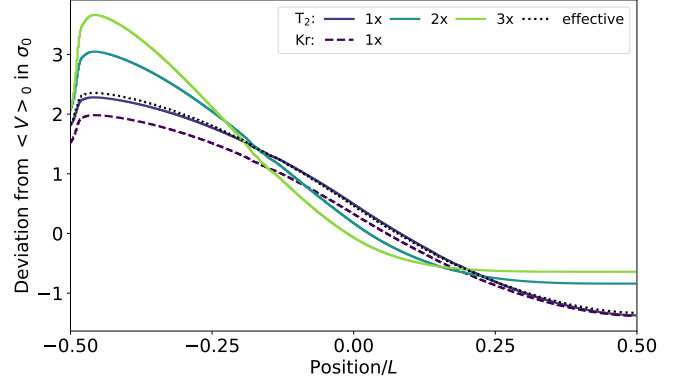


Fig. 6: Maximum solution. Shown are the potential shapes $Q_i(z)$ that lead to the maximum energy-loss shifts for the scattering multiplicities 1x, 2x and 3x for tritium electrons, and 1x for krypton electrons. The "effective" shape combines the contributions from all scatterings, considering their relevance for the tritium β spectrum (c.f. section 4.5). In the 40 eV analysis window of the β spectrum, the effective shape is strongly dominated by 1x scattering. The source conditions of the KATRIN measurement campaigns since KNM3-NAP (c.f. table 1) have been used.

to arbitrary numbers of scattering i . The standard deviation σ_0 of the non-scattered electron distribution is used here for brevity, but any other one works the same way. This and more generalizations are discussed in [6] alongside other constraints of for example the peak-to-peak value of the potential by the measured observables.

Using the weighted covariance

$$\text{Cov}_k[F, G] = \langle FG \rangle_k - \langle F \rangle_k \langle G \rangle_k, \quad (28)$$

one can write the energy-loss shifts as

$$\Delta_{10}[V] = \text{Cov}_0 \left[\frac{P_i - P_0}{P_0}, V \right]. \quad (29)$$

This is shown using $\langle F \rangle_0 = \langle FP_0 \rangle$ and the fact that $\langle P_i - P_0 \rangle = 0$ due to the normalization of the $P_i(z)$. Thus, the second term vanishes when one expands the covariance in equation 29. The goal is now to derive a measure of correlation from equation 29. First, the scalar covariances of the electron distributions are introduced as

$$\kappa_{ij} \equiv \text{Cov}_0 \left[\frac{P_i - P_0}{P_0}, \frac{P_j - P_0}{P_0} \right], \quad (30)$$

with $\kappa_{ii} \equiv \kappa_i^2$.

By normalizing equation 29 by the standard deviation of the arguments on the right side, one obtains the shape operators

$$\hat{\rho}_i[V] \equiv \frac{\text{Cov}_0 \left[\frac{P_i - P_0}{P_0}, V \right]}{\sigma_0 \left[\frac{P_i - P_0}{P_0} \right] \sigma_0[V]} = \frac{1}{\kappa_i} \frac{\Delta_{10}}{\sigma_0} [V]. \quad (31)$$

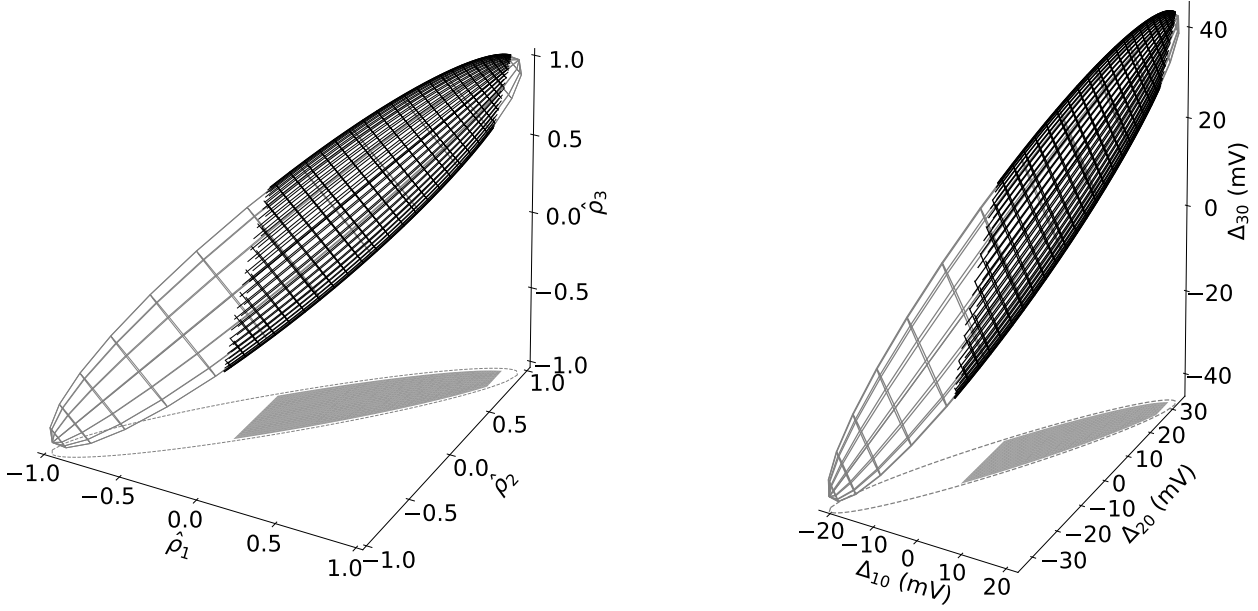


Fig. 7: Parameter spaces. The left plot shows the high correlation of the $\vec{\rho}$ parameter space: the major axis of the ellipsoid is oriented almost perfectly along the diagonal, such that high (low) values of one $\hat{\rho}_i$ correspond to high (low) values of the other $\hat{\rho}_j$. In the right plot the ellipsoid is rescaled to represent the $\vec{\Delta}$ parameter space, constrained by a measured value of $\sigma_0 \approx 32$ mV [11]. The constraint weakens for higher scatterings, since the overlap of the respective electron distribution with the one of the unscattered electrons decreases. Shaded in black, the 1σ region constrained by a ^{83m}Kr measurement of $\Delta_{10} = (11 \pm 7)$ mV is shown, where the central value was chosen arbitrarily. The uncertainty is motivated by the already recorded experimental data. The constraint considers the difference between the T_2 and ^{83m}Kr Δ_{10} , as discussed in section 4.3.

Since the left side defines a correlation, which is bounded in the interval $[-1, 1]$, it holds for any arbitrary potential that

$$|\Delta_{i0}[V]| \leq \kappa_i \sigma_0[V]. \quad (32)$$

The equal sign holds for the potentials

$$\frac{V(z) - \langle V \rangle_0}{\sigma_0} = \pm \underbrace{\frac{1}{\kappa_i} \frac{P_i - P_0}{P_0}}_{\equiv Q_i(z)}(z), \quad (33)$$

which directly follows from equation 31, using that the covariance of the constant term $\langle V \rangle_0$ vanishes. The $\hat{\rho}_i$ measure the correlation to this potential shape $Q_i(z)$, and thus the absolute value of Δ_{i0} is larger on the scale of σ_0 , when the potential is similar to equation 33.

A plot of the $Q_i(z)$ is shown in figure 6. Qualitatively, non-scattered electrons stem from the front side of the WGTS, while scattered electrons stem from the rear side, such that antisymmetric potentials with respect to the central injection point maximize $|\Delta_{i0}|$ for a given σ_0 . Symmetric potentials with regard to the injection point do not produce large $|\Delta_{i0}|$ compared to σ_0 .

Relations for arbitrary number of scatterings

For KATRIN more than one scattering is relevant. Now, the image $\vec{\rho}[V] = (\hat{\rho}_1 \hat{\rho}_2 \dots)^T[V]$ is bounded for any V . Since the Δ_{i0} are linear, one obtains the boundary potentials as linear combination of the one-dimensional solutions

$$\frac{V(z) - \langle V \rangle_0}{\sigma_0} = \vec{a} \vec{Q}(z), \quad (34)$$

where \vec{a} is the coefficient vector. Its normalization is determined by calculating $\sigma_0[\dots]$ of equation 34. Using the scalar correlations

$$\rho_{ij} \equiv \frac{\kappa_{ij}}{\kappa_i \kappa_j}, \quad (35)$$

$$= \hat{\rho}_i[Q_j], \quad (36)$$

with corresponding correlation matrix \mathbf{P} , basic algebra of covariances and equation 36, it can be shown that

$$\sigma_0[\vec{a} \vec{Q}] = \sqrt{\vec{a}^T \mathbf{P} \vec{a}}, \quad (37)$$

$$\vec{\rho}[\vec{a} \vec{Q}] = \frac{\mathbf{P} \vec{a}}{\sqrt{\vec{a}^T \mathbf{P} \vec{a}}}, \quad (38)$$

Table 1: Standard deviations κ_i and correlations ρ_{ij} of the weight functions for the different KATRIN measurement campaigns KNMx. The last column indicates which value of σ_0 must be used together with the coefficients. The reason for this is explained in section 4.3. The values of the column density (CD) are relative to the nominal value of $5 \cdot 10^{21} \frac{1}{\text{m}^2}$.

Measurement campaign	Configuration (CD, Temp)	κ_1	κ_2	κ_3	ρ_{12}	ρ_{13}	ρ_{23}	value of σ_0 from
KNM1	20 %, 30 K	0.62	0.97	1.23	0.97	0.91	0.98	T_2
KNM2	84 %, 30 K	0.75	1.23	1.62	0.96	0.89	0.98	T_2
KNM3-SAP	40 %, 80 K	0.62	0.97	1.23	0.96	0.90	0.98	$^{83\text{m}}\text{Kr}$
Since KNM3-NAP	75 %, 80 K	0.69	1.09	1.38	0.96	0.89	0.98	$^{83\text{m}}\text{Kr}$

holds. Since $\sigma_0[\dots]$ applied to the left side of equation 34 is 1, \vec{a} needs to be chosen such that

$$\vec{a}^T \mathbf{P} \vec{a} = 1. \quad (39)$$

Now, using the inverse of the correlation matrix \mathbf{P}^{-1} and equations 38 and 39, the coefficient vector of the boundary potentials is determined to be

$$\vec{a} = \mathbf{P}^{-1} \vec{\rho} \quad (40)$$

and the boundary of $\vec{\rho}$ is given by

$$1 = \vec{\rho}^T \mathbf{P}^{-1} \vec{\rho}. \quad (41)$$

Since the correlation matrix is positive definite, this parametrizes an ellipsoid, which is shown in figure 7. A maximum of 3 scatterings is shown, with correlations derived from the electron distributions at the source density that was used since the KNM3-NAP neutrino-mass measurement campaign at KATRIN. Values of the covariances and correlations of the weight functions are shown in table 1.

3 Effect of the source potential on the T_2 -spectrum observables

The goal of this section is to derive equations for the leading order changes of the observed tritium spectrum endpoint ΔE_0 and the squared neutrino mass Δm^2 , caused by an unknown starting potential. The main sources on this topic [10, 12] do not consider electron scattering and thus do not account for a possible bias caused by energy-loss shifts $\Delta_{i0}[V]$. To do so, the response function of KATRIN has to be considered, which leads to a very complex discussion. Thus, the aim of this section is to gain a qualitative understanding rather than a quantitative one, and to show, that there are significant deviations to the previous understanding of this kind of systematic bias on the neutrino mass. The quantitative assessment is best done on Asimov Monte Carlo studies on the detailed model, as in [6].

3.1 Small energy fluctuations of the intrinsic β spectrum

It is long established, that the leading order bias of the squared neutrino mass, caused by an unrecognized Gaussian energy distribution convolved with the tritium β spectrum, is given by $\Delta m^2 = -2\sigma^2$, where σ^2 is the variance of the distribution [12]. Naturally, the endpoint is shifted by the mean μ of the distribution $\Delta E_0 = \mu$. In [10], Slezak showed these relations for an arbitrary, normalized energy distribution f and also concluded, that the next higher moment, the skewness, has no additional effect on ΔE_0 and Δm^2 .

Thus, for the intrinsic β spectrum, following from [10] the leading order shifts are

$$\begin{aligned} \Delta E_0 &= \mu[f], \\ -\frac{\Delta m^2}{2} &= \sigma^2[f], \end{aligned} \quad (42)$$

where

$$\begin{aligned} \mu[f] &\equiv \int d\epsilon \epsilon f(\epsilon), \\ \sigma^2[f] &\equiv \int d\epsilon (\epsilon - \mu[f])^2 f(\epsilon), \end{aligned} \quad (43)$$

are the mean and central variance of the distribution f .

Slezak derives the factors ϵ, ϵ^2 in the integrals of equation 43 from the Taylor expanded β spectrum for small neutrino mass. However, as visible in figure 8, to be fully precise these integrals need to contain the energy cut by the endpoint $\Theta(E_0 - m - E + \epsilon)$, such that the boundaries can come either from the endpoint, or from the energy distribution f . The transition happens at energies where $E_0 - m - E \lesssim \sigma[f]$. If $\sigma[f]$ is small, for example on a sub eV scale, then this subtlety really only arises so close to the endpoint, that it is statistically insignificant given the small rate in this region and that is what [10] implicitly uses. However, when the response function is introduced, the cut by the endpoint becomes important, as discussed in the following.

3.2 Systematic bias as moments of the response function

Despite of the sign of the integration variable, the integration over the response function as in equation 8 is the same

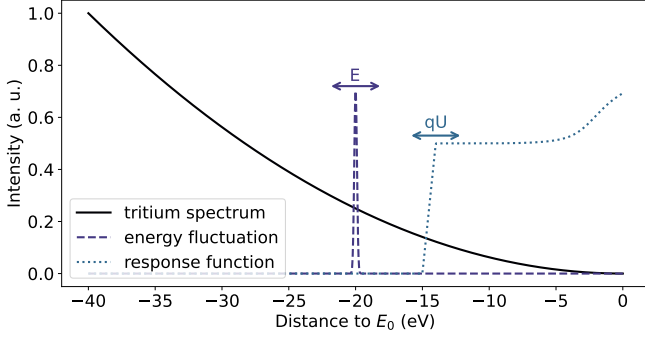


Fig. 8: Integrations over the tritium spectrum. In the convolution with an energy fluctuation, the spectrum is averaged around the selected energy E , weighted with the fluctuation. Since the width of the fluctuation is small, the cut by the β spectrum is only relevant for energies E very close to the endpoint E_0 . In contrast, the integration over the response function depends on the upper cut of the β spectrum for every qU .

operation as the convolution with an energy fluctuation. Ultimately, in order to derive the shift of the β spectrum observables caused by an unrecognized modification of the response function in leading order, at some point the Taylor expansion of the spectrum introduced in [10] has to be used, again leading to the equations 42, only that the energy fluctuation is replaced by the response function.

However, to do so, the limits of the integrals have to be considered. As visible in figure 8, since the upper cut always comes from the endpoint, it is sufficient that the response function vanishes at the lower side. One can then define the moments of the response function R like

$$\begin{aligned} N[R] &= \int^{E_0-m} dE R(E), \\ \mu[r] &= \int^{E_0-m} dE E r(E), \\ \sigma^2[r] &= \int^{E_0-m} dE (E - \mu[r])^2 r(E), \end{aligned} \quad (44)$$

where r is R divided by the norm $N[R]$ of R . $N[R]$ is only a scaling factor, which can be absorbed by a nuisance parameter of the β spectrum intensity. These moments implicitly depend on U via the response function.

Fitting a model using a response function r without potential to data with response r' , that includes the potential, one then obtains the shifts

$$\begin{aligned} \Delta E_0 &= \langle \mu[r] - \mu[r'] \rangle_U, \\ -\frac{\Delta m^2}{2} &= \langle \sigma^2[r] - \sigma^2[r'] \rangle_U, \end{aligned} \quad (45)$$

as average over all U . Here, some major differences to the shifts obtained for the intrinsic β spectrum (equations 42)

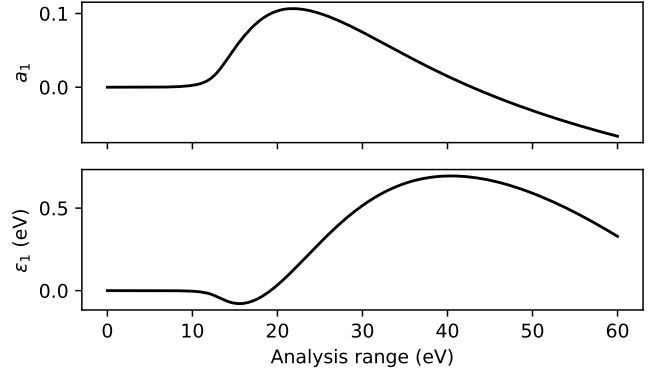


Fig. 9: Susceptibility of endpoint (top) and squared neutrino mass (bottom) to an unaccounted Δ_{10} vs. analysis range. Shown are the first derivatives of the shifts ΔE_0 and Δm^2 with regard to an unaccounted Δ_{10} (c.f. equations 46). The shifts were calculated from equations 52 using an approximate response model. Compared to the full simulation in [6], good qualitative agreement is observed for the case of ϵ_1 . In contrast, while the scale of a_1 is correct, the position of its maximum deviates visibly, possibly due the approximations of the analytical calculation.

are visible: The weighting of the U -average has to contain the distribution of measurement time to the retarding potentials, such that the bias does depend on the measurement conditions². This is expected, since a modification of the response function in for example the energy loss model can only affect the measurement, if scattered electrons are part of the measurement time distribution. Also, in contrast to equations 42, where the shift of the squared neutrino mass is always negative, in equation 45 it can also be positive.

3.3 Leading order calculation

Evaluating equations 45 analytically is very challenging. To simplify the process they are linearized. Thus, the goal is to derive the leading order coefficients

$$\begin{aligned} a_i &\equiv \frac{1}{q} \frac{dE_0}{d\Delta_{i0}}, \\ \epsilon_i &\equiv \frac{1}{q} \frac{dm^2}{d\Delta_{i0}}, \end{aligned} \quad (46)$$

i.e. the first derivative of the endpoint and squared neutrino mass with regard to Δ_{i0} . Since the calculation is very technical and the results are only qualitative, only the basic ideas are described here. $q = -1$ is used in the following.

²Also, usually the observables are derived from a χ^2 minimum, in which case the weight also contains the normalized derivative of the integrated spectrum with regard to each observable. This gives a system of equations, which modifies the results compared to equations 45.

Normalization: The upper integration boundary of the response moments (equations 44) depends on the bias of the endpoint and the squared neutrino mass. It is assumed, that the dependency on the neutrino mass is covered by the background. To compensate for the remaining dependency, a correction term proportional to the endpoint is added to the final results. It is calibrated with the case of a constant potential $V(z) = \langle V \rangle_0$, where the endpoint bias is just the potential $\Delta E_0 = q \langle V \rangle_0$ and the neutrino mass bias vanishes.

Energy dependency: It is assumed that the response function only depends on the surplus energy $\varepsilon \equiv E - qU$. In this case all integrals can be rewritten as function of the surplus energy and the distance $\Delta qU = E_0 - m - qU$ of the retarding energy to the endpoint. The integrals of equation 44 can then be reformulated in the range of $[0, \Delta qU]$. Thereby one finds that the mean $\mu[r]$ scales linearly with qU , and it is convenient to replace it by

$$\tilde{\mu}[r] \equiv \mu[r] - qU. \quad (47)$$

Linear combination: Since the response function is a summation of response functions of different scatterings R_i , the same holds for the shifts ΔE_0 and Δm^2 , which then depend on moments of the normalized response like $N_i \equiv N[r_i]$, $\tilde{\mu}_i \equiv \tilde{\mu}[r_i]$ etc.

Expansion: The modified response functions for each scattering are expanded in orders of the potential

$$\langle R_i(E, U - V(z)) P_i(z) \rangle = \sum_{n=0}^{\infty} \frac{R_i^{(n)}(E, U)}{n!} (-1)^n \langle V^n \rangle_i. \quad (48)$$

$R_i^{(n)}$ is the n -th derivative with regard to U . The change of the normalized response with $\Delta_{i0}[V]$ is then

$$\frac{dr}{d\Delta_{i0}} = \frac{R_i^{(1)}}{N[R]} - r \frac{N[R_i^{(1)}]}{N[R]}, \quad (49)$$

$$\equiv r_i^{(1)} - r N[r_i^{(1)}], \quad (50)$$

where it is important to consider, that both the response and the normalization depend on Δ_{i0} . The normalization of the first derivative $N[r_i^{(1)}]$ is just the response $r_i(\Delta qU)$ itself. Using integration by parts on some of the integrals, combining all the steps and omitting the arguments $[r]$ and $[r_i]$, one then finds the leading order shifts

$$\begin{aligned} \Delta E_0^{(1)} &= -\langle V \rangle_0 - \sum_{i=1} a_i \Delta_{i0}[V], \\ \Delta m^2^{(1)} &= -\sum_{i=1} \varepsilon_i \Delta_{i0}[V], \end{aligned} \quad (51)$$

where

$$a_i = \frac{\langle N_i - \mathcal{E} r_i \rangle_{\Delta qU}}{\langle 1 - \mathcal{E} r \rangle_{\Delta qU}}, \quad (52)$$

$$\varepsilon_i = \langle 4\mathcal{E} N_i - 4\mathcal{E}_i + 2\mathcal{V}(a_i r - r_i) \rangle_{\Delta qU}.$$

The new quantities are defined and discussed in the following. The asymptotic behavior of the normalized response r_i and the normalization N_i is related to the weighted scattering probabilities \bar{p}_i (equation 5)

$$\lim_{\Delta qU \rightarrow \infty} r_i \propto \frac{\bar{p}_i}{\Delta qU}, \quad (53)$$

$$\lim_{\Delta qU \rightarrow \infty} N_i \propto \bar{p}_i. \quad (54)$$

The normalization N_i can be interpreted as the fraction of measured surplus energy of i -times scattered electrons.

Both coefficients in equation 52 depend on a measure of the mean measured surplus energy of i -times scattered electrons

$$\mathcal{E}_i \equiv N_i \Delta qU - \tilde{\mu}_i, \quad \lim_{\Delta qU \rightarrow \infty} \mathcal{E}_i \propto \Delta qU \bar{p}_i. \quad (55)$$

Additionally, ε_i depends on a measure of the variance of the measured surplus energy

$$\mathcal{V} \equiv \mathcal{E}^2 - \sigma^2, \quad \lim_{\Delta qU \rightarrow \infty} \mathcal{V} \propto \Delta qU^2. \quad (56)$$

An evaluation of equations 52 using a simplified response model and an unweighted ΔqU -averaging is shown in figure 9 as function of the analysis range of the β spectrum. Both graphs show a non-trivial structure. Comparing to [6], where the same coefficients were studied with fits on Asimov spectra, the order of magnitude is in agreement and the position of the visible maximum is agreeing for ε_1 . In contrast, the position of the maximum of a_1 does not agree with the simulation, possibly due to approximations of the calculation shown here.

3.4 Interpretation

Since the response function is not a density function, the meaning of the moments and the derived expressions 52 is not intuitive. Nevertheless, these equations are still useful to understand figure 9.

As it should be expected, a_i and ε_i are only non-vanishing, if the respective scattering multiplicity is contained in the measurement time distribution.

The averaging over ΔqU entails an integration, such that the expressions inside the averages are proportional to the derivatives of figure 9. Asymptotically, the expressions inside the averages scale with \bar{p}_i in case of the endpoint and $\Delta qU \bar{p}_i$ in case of the squared neutrino mass. However, since the response function varies on a scale of several 10 eV, the

asymptotic behavior is not reached in the plotted range, such that the curves do depend on the details of the response model. Also, the integration of the ΔqU -average raises the exponent of ΔqU by one. In the exemplary case of a_i this means, that the dependency on the analysis range does not vanish even for large ΔqU , and the a_i do not converge to \bar{p}_i , as it might be naively assumed. This is a result of the integral measurement at KATRIN, since a data point at qU depends on the whole spectrum for energies larger than qU .

Due to the complexity, the second order terms have not been investigated analytically. However, since the energy-loss function has a width that is orders of magnitudes larger than the standard deviations of the potential, only σ_0 is relevant, which was also found in the simulations of [6].

Overall, the linear order shifts of E_0 and m^2 occur because of a wrongly predicted mean and variance of the measured surplus energy. The order of magnitude of the coefficients is obtained by \bar{p}_i in case of the endpoint, and $\Delta qU \bar{p}_i$ in case of the squared neutrino mass. Given the analysis range on the 10 eV scale and scattering probabilities in the 10 % regime, ε_i is on the 1 eV scale, such that the squared neutrino mass is very susceptible to Δ_{10} .

4 Supplements

The following sections discuss further details, which are relevant for the previous discussions.

4.1 Higher-order effects

In this section several higher-order effects are discussed, that were neglected in the derivation of the main text.

Energy and angle dependency of the electron distributions

In the main text the energy and angle dependency of the electron distributions is neglected, and instead they are evaluated at a fixed energy E_{fix} and with scattering probabilities averaged over the angle.

The dependency on the energy is very small and also mitigated by the fact, that depending on the multiplicity of scattering, the initial energy of the electron can only deviate by a certain amount from E_{fix} , otherwise the electron is scattered outside of the analysis range. This leads to a maximum spread of the initial energy of

$$\Delta E = 40 \text{ eV} - i \times 13 \text{ eV} \quad (57)$$

for an electron, that is scattered i -times. Here 40 eV is a typical analysis range and 13 eV the approximate minimum energy loss in one scattering event. Accordingly, unscattered electrons can have a spread in initial energy of 40 eV, while

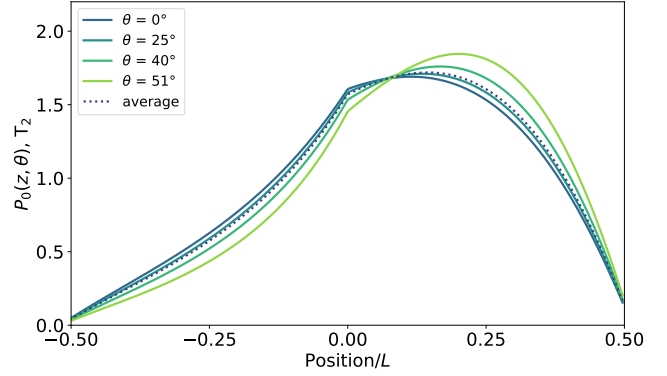


Fig. 10: Dependency of the unscattered electron distribution on the angle. The electron distributions $P_0(\theta, z)$ are a function of $\cos \theta$. Accordingly, the change with θ increases, when θ is larger. Electrons with a large angle are more likely to stem from the front of the source, compared to electrons with a small angle.

the (for the 40 eV range) maximally allowed 3-times scattered electrons have a spread of only 1 eV.

The effect of the angle on the other hand, is more pronounced. Figure 10 shows the distribution of the unscattered electrons for T_2 depending on the angle. For large angles there is a visible change of the distributions, and thus of the sensitive region to the potential.

One can quantify the uncertainty resulting from the visible spread in the electron distribution using methods already developed in the main text. Using a Taylor expansion of the response function equation 9 and calculating the maximum difference for the smallest and largest possible angle, the first order correction term is proportional to

$$\Delta_\theta[V] \equiv \langle V P_0(\theta = \theta_{\text{max}}) \rangle - \langle V P_0(\theta = 0) \rangle, \quad (58)$$

$$\equiv \langle V P_{\Delta\theta} \rangle. \quad (59)$$

Analogous to section 2.3 and equation 32, given a measured scale $\sigma_0[V]$ of the potential inhomogeneity, $\Delta_\theta[V]$ is bounded by

$$|\Delta_\theta[V]| \leq \kappa \sigma_0[V]. \quad (60)$$

The potential, that produces the largest effect, is given by

$$Q(z) = \frac{1}{\kappa} \frac{P_{\Delta\theta}}{P_0}(z), \quad (61)$$

and the coefficient $\kappa \approx 0.2$ is the standard deviation of $\frac{P_{\Delta\theta}}{P_0}$. Neglecting phase space factors in θ , and assuming the unlikely case that the potential is finely tuned according to equation 61, this represents the maximum relative uncertainty of the first potential moments. While further studies are required to determine a fully conclusive value, it is plausible that this uncertainty is significantly overestimated.

Moreover, as demonstrated in this work, the primary sensitivity of the neutrino-mass measurement to the source potential originates from $\Delta_{10}[V]$. The effect discussed here constitutes an additional modification of the transmission edge, resulting in a neutrino-mass bias that is smaller by approximately an order of magnitude.

Inhomogeneity of the source magnetic field

In principle, the electron distributions $P_i(z)$ must account for all z -dependent quantities that affect the rate of the electrons. One additional z -dependency worth mentioning arises from a slight decrease of the source magnetic field between the coils. Its impact on the electron rate is governed by two opposing effects: On the one hand, the magnetic field determines the volume of the flux tube; on the other hand, it sets the maximum pitch angle of the electrons, beyond which they are intentionally reflected by a strong magnetic field in front of the detector. As visible in figure 3, the influence of the inhomogeneity of the source magnetic field on the electron distributions is very small, and can be neglected. Usually a constant, effective value is used, which is designed to compensate the neutrino-mass bias from the then neglected z -dependency [3].

4.2 Parameterizing the Δ -parameter space and coverage

Equation 41 is a quadratic equation with a positive and negative solution. For the first 3 scatterings the volume enclosed by the solution can be parametrized using parameters $r_i \in [-1, 1]$ like

$$\hat{\rho}_1 = r_1, \quad (62)$$

$$\hat{\rho}_2 = \hat{\rho}_1 \rho_{12} + r_2 \sqrt{(1 - \rho_{12}^2)(1 - \hat{\rho}_1^2)}, \quad (63)$$

$$(1 - \rho_{12}^2)\hat{\rho}_3 = \hat{\rho}_1(\rho_{23}\rho_{12} - \rho_{13}) - \hat{\rho}_2(\rho_{13}\rho_{12} - \rho_{23}), \quad (64)$$

$$+ r_3 \sqrt{|\mathbf{P}| [(1 - \hat{\rho}_1^2)(1 - \hat{\rho}_2^2) - (\rho_{12} - \hat{\rho}_1\hat{\rho}_2)^2]}, \quad (65)$$

with determinant

$$|\mathbf{P}| = (1 - \rho_{13}^2)(1 - \rho_{23}^2) - (\rho_{12} - \rho_{13}\rho_{23})^2. \quad (66)$$

The resulting $\vec{\rho}$ is translated to $\vec{\Delta}$ using equation 31, and those values are used to shift the convolved energy-loss function 2.

The usage of bounded parameters can produce complications regarding the treatment of uncertainties and the coverage. It has been shown in Monte Carlo studies that in order to obtain correct coverage, in addition to the necessary boundaries in the interval $[-1, 1]$, a Gaussian pull term should be set on the r_i , centered at 0 and with a standard deviation of 1.

4.3 Differences of T_2 and ^{83m}Kr and measurement of Δ_{10}

Due to the different gas profiles of T_2 and ^{83m}Kr , the moments of the starting potential that both spectra observe are different even for the same potential.

In the treatment of the Δ_{10} the translation between the gas species is considered by calculating the covariances κ_{ij} accordingly. In the KNM1&2 measurement campaigns the T_2 and ^{83m}Kr measurement were taken at different source conditions, possibly affecting the source potential. This is considered in [11] by drastically increasing the uncertainty of σ_0 . It can then be interpreted as the value observed by the T_2 electrons, such that the limits on $|\Delta_{10}|$ from equation 32 have to use the T_2 electron distribution $P_0(z)$ in the denominator of the $Q_i(z)$.

In all other campaigns, the T_2 and ^{83m}Kr measurements are taken at the same source conditions. Since the neutrino-mass bias caused by the broadening is small, the scaling of σ_0 from ^{83m}Kr to T_2 can be neglected. Also, as shown in [6] the uncertainty in this scaling is larger, when the absolute value of $\hat{\rho}$ is smaller; in this case the neutrino mass bias is dominated by the component related to $\hat{\rho}$ anyway. Then, σ_0 from the ^{83m}Kr measurement can directly be used in equation 32 to constrain the Δ_{10} , such that the distribution $P_0(z)$ of the ^{83m}Kr electrons is used in the denominator of the $Q_i(z)$.

In all cases, the difference $P_i(z) - P_0(z)$ in the numerator of the $Q_i(z)$ is taken from the T_2 electron distributions, since the T_2 Δ_{10} should be constrained. Rescaling the $\hat{\rho}$ -ellipsoid to a Δ -ellipsoid is always done using the κ_i coefficients for T_2 .

The measurement of Δ_{10} and σ_0 in ^{83m}Kr allows to calculate $\hat{\rho}_1$ of krypton using equation 31 and the value of $\kappa_{1,\text{Kr}}$ for the T_2 column density used in the ^{83m}Kr measurement. $\hat{\rho}_1$ is then used to constrain the respective value of tritium following from equation 63 by

$$\hat{\rho}_{1,T2} = \hat{\rho}_{1,\text{Kr}}\rho_{11,\text{Kr}T2} \pm \sqrt{(1 - \rho_{11,\text{Kr}T2}^2)(1 - \hat{\rho}_{1,\text{Kr}}^2)}, \quad (67)$$

where the correlation $\rho_{11,\text{Kr}T2}$ between the ^{83m}Kr and T_2 $P_1(z) - P_0(z)$ is used. This value of $\hat{\rho}_{1,T2}$ is then the input of equation 62. In the case where the measurement fluctuates close to a boundary of the allowed parameter space, further coverage studies might be required. The κ and ρ values for the translation are shown in table 2. Only the values for the

Table 2: Standard deviation $\kappa_{1,\text{Kr}}$ and correlation $\rho_{11,\text{Kr}T2}$ for the translation between the ^{83m}Kr and T_2 measurement in the 75 % measurement.

Measurement campaign	Configuration (CD, Temp)	$\kappa_{1,\text{Kr}}$	$\rho_{11,\text{Kr}T2}$
Since KNM3-NAP	75 %, 80 K	0.73	0.95

75% measurement are shown, since here the same conditions are used for $^{83\text{m}}\text{Kr}$ and T_2 , such that the source potential can be assumed to be the same. If this is not given, then Δ_{10} cannot be translated between the two spectra without further assumptions, which is the case for all other measurement campaigns.

The limit on the T_2 Δ_{10} by equation 32 and the measured broadening $\sigma_0 \approx 32$ mV is around 22 mV [11] for the last neutrino-mass campaigns. The projected uncertainty on the $^{83\text{m}}\text{Kr}$ Δ_{10} is around 7 mV, which would be a factor 3 smaller. Unfortunately, even though the T_2 and $^{83\text{m}}\text{Kr}$ Δ_{10} are very highly correlated, the translation by equation 67 adds a significant amount of uncertainty to the T_2 value. The largest increase happens, when the central value is 0, resulting in a symmetrical T_2 uncertainty of 13 mV. If the central value of $|\Delta_{10}|$ is larger, for example 13 mV, the resulting $\pm 1 \sigma$ interval of the tritium value is still $[-2 \text{ mV}, +22 \text{ mV}]$, allowing to constrain approximately half of the parameter space. Only when the measured $^{83\text{m}}\text{Kr}$ $|\Delta_{10}|$ is very large the size of the $T_2 \pm 1 \sigma$ interval approaches that of the $^{83\text{m}}\text{Kr}$ measurement.

4.4 Dependency of z -averaged quantities on the gas profile

The covariances κ_{ij} and correlations ρ_i are important factors in quantifying the neutrino-mass bias caused by the source potential. They are obtained by calculating averages of the z -dependent electron distributions $P_i(z)$. For the case of T_2 , these averages do not depend on the detailed shape of the density profile, but only on the total column density³, making them robust against uncertainties in the modeling or in variations of source properties like the temperature.

This can be understood by noting that the scattering probabilities (c.f. equation 3) depend only on the effective column density $\mathcal{N}_{\text{eff}}(\theta, z)$, which itself is an integral over the density profile. Consequently, integrals over z involving the density profile can be substituted by integrals over the effective column density.

However, in the case of $^{83\text{m}}\text{Kr}$, this simplification does not apply. While the scattering probabilities are still governed by the T_2 density, the electron distributions $P_i(z)$ are directly proportional to the $^{83\text{m}}\text{Kr}$ density.

4.5 Effective treatment of the Δ -parameter space

The first order bias of the squared neutrino mass is given by

$$\Delta m^2 = - \sum_{i=1} \varepsilon_i \Delta_{i0} . \quad (68)$$

³Thanks to F. Glück for pointing this out!

If the susceptibilities ε_i are known, then an effective Δ_ρ can be defined like

$$\Delta_\rho \equiv \frac{1}{\varepsilon} \sum_{i=1} \varepsilon_i \Delta_{i0} , \quad (69)$$

such that the bias of the squared neutrino mass is given by

$$\Delta m^2 = -\varepsilon \Delta_\rho . \quad (70)$$

The normalization ε determines how the effective Δ_ρ is used in the model. If all Δ_{i0} are shifted equally by Δ_ρ , then it follows from equation 68 that ε is the sum of the ε_i .

By construction, this approach gives the correct bias of the squared neutrino mass, but it has many disadvantages:

- The ε_i have to be determined beforehand, which is usually done in Asimov studies neglecting correlations to other systematic effects and using a simplified analysis.
- Since the ε_i depend on the performed analysis, different values of Δ_ρ have to be used for different analyses. This will be especially noticeable when changing the analysis range, leading to a large change of Δ_ρ .
- Even if the ε_i are correct for the given analysis, only the neutrino mass bias is compensated. The bias of the other observables and the residual structure caused by non-vanishing Δ_{i0} remains or can even be amplified.

Therefore, it is strongly recommended to treat the entire parameter space correctly, using the equations presented in section 4.2.

5 Conclusions and outlook

For KATRIN to reach its sensitivity goal, a careful assessment of systematic biases is required. This work investigated the bias caused by inhomogeneities in the source potential, demonstrating that the resulting effects are significantly larger than those accounted for in KATRIN's predecessor experiments. These effects were discussed in leading order and the corresponding observables of the starting potential were derived. In particular, due to the existence of electron scattering, the leading order neutrino mass bias by the inhomogeneity of the potential is in contrast to the previous belief not caused by a Gaussian broadening $\sigma_0[V]$, but by mutual shifts $\Delta_{i0}[V]$ of the spectra of different scattering multiplicities. Since this effect produces residuals not at the endpoint, but starting from $\approx 13 \text{ eV}$ deep into the spectrum, its possible neutrino-mass bias is many factors larger than expected simply by a Gaussian description. It was motivated in this work why the bias scales with approximately $\Delta m^2 \propto 1 \text{ eV} \cdot \Delta_{10}$. It was also shown that the parameter space of the Δ_{i0} is an ellipsoid constrained by the standard deviation σ_0 of the potential, and that the boundary of the ellipsoid is produced by source potentials that are asymmetric

with regard to the injection point in the center of the source. To constrain the parameter space further, the $^{83\text{m}}\text{Kr}$ measurement is used, where the effect of asymmetric potentials is directly visible as a shift between the 1x scattered and unscattered line. The experimental approach of the $^{83\text{m}}\text{Kr}$ measurement is described in a parallel publication [11], where $\sigma_0^2 = 1.0(3) \times 10^{-3} \text{ eV}^2$ is determined, leading to a systematic neutrino-mass uncertainty on the order of $2 \times 10^{-2} \text{ eV}^2$. In the future the already recorded measurement of Δ_{10} will be analyzed, and as shown in this work, it is foreseen that it will allow to reduce the systematic bias on the neutrino mass further by a factor of around 2 to 3, depending on the central value of the measured Δ_{10} .

Acknowledgements I would like to thank M. Böttcher, M. Kleesiek, M. Schlösser, M. Slezák, A. Lokhov and K. Valerius for the helpful discussions and support. Furthermore I thank C. Fengler, J. Štorek and F. Glück for the review of the manuscript.

References

1. Y. Fukuda et al. *Phys. Rev. Lett.*, 82:2644–2648, 1999. doi:[10.1103/PhysRevLett.82.2644](https://doi.org/10.1103/PhysRevLett.82.2644).
2. Q. R. Ahmad et al. *Phys. Rev. Lett.*, 89(1):011301, 2002. doi:[10.1103/PhysRevLett.89.011301](https://doi.org/10.1103/PhysRevLett.89.011301).
3. KATRIN Collaboration. *Science*, 388(6743):180–185, 2025. doi:[10.1126/science.adq9592](https://doi.org/10.1126/science.adq9592).
4. M. Aker et al. *J. Instrum.*, 16(08):T08015, 2021. doi:[10.1088/1748-0221/16/08/T08015](https://doi.org/10.1088/1748-0221/16/08/T08015).
5. M. Kleesiek et al. *Eur. Phys. J. C*, 79(3):204, 2019. doi:[10.1140/epjc/s10052-019-6686-7](https://doi.org/10.1140/epjc/s10052-019-6686-7).
6. M. B. Machatschek. *A Phenomenological Theory of KATRIN Source Potential Systematics and its Application in Krypton-83m Calibration Measurements*. PhD thesis, KIT, 2021. URL <https://doi.org/10.5445/IR/1000132391>.
7. D. Kalempa and F. Sharipov. Separation phenomenon in the windowless gaseous tritium source of katrin experiment. ternary mixtures, 2010. URL <http://fisica.ufpr.br/sharipov/KATRIN/report5.pdf>. Accessed 17 April 2025.
8. M. Hötzel. *Simulation and analysis of source-related effects for KATRIN*. PhD thesis, KIT, 2012. URL <https://doi.org/10.5445/IR/1000031259>.
9. S. Groh. *Modeling of the response function and measurement of transmission properties of the KATRIN experiment*. PhD thesis, KIT, 2015. URL <https://doi.org/10.5445/IR/1000046546>.
10. M. Slezák. *Monitoring of the energy scale in the KATRIN neutrino experiment*. PhD thesis, Prague, Inst. Phys., 2016. URL <https://cds.cern.ch/record/2243754>.
11. H. Acharya et al. arXiv:2503.13221, 2025. doi:<https://doi.org/10.48550/arXiv.2503.13221>.
12. R. G. H. Robertson and D. A. Knapp. *Annu. Rev. Nucl. Part. Sci.*, 38:185–215, 1988. doi:[10.1146/annurev.ns.38.120188.001153](https://doi.org/10.1146/annurev.ns.38.120188.001153).